The Visualization and Measurement of Left Ventricular Deformation

Burkhard Wünsche

Department of Computer Science
University of Auckland,
Private Bag 92019, Auckland, New Zealand
Email: `burkhard@cs.auckland.ac.nz`

Abstract

While medical progress has been made in the diagnosis and treatment of heart diseases it remains the biggest killer in the western world. Cardiovascular diseases cause considerable morbidity and the prognosis after heart failure is poor. An improved understanding of cardiac mechanics might advance the diagnosis and treatment of heart diseases.

We have developed a toolkit designed for visualizing biomedical models. This paper explains techniques for visualizing and evaluating biomedical finite element models and demonstrates their application to biomedical data sets by using as an example two models of a healthy and a diseased human left ventricle.

The contributions of this paper are threefold: First we apply techniques traditionally used in solid mechanics and computational fluid dynamics to biomedical data. We also suggest some minor improvements and modifications. Secondly we obtain new insight into the mechanics of the healthy and diseased left ventricle and we facilitate the understanding of the complex deformation of the heart muscle by novel visualizations. Finally we also introduce in this process a toolkit designed for visualizing biomedical data sets.

Keywords: Scientific Visualization, Visualization Tools, Strain Tensor Field, Finite Element Model, Cardiac Mechanics.

1 Introduction

Heart disease remains the biggest killer in the western world (Masood, Yang, Pennell & Firmin 2000). One or multiple heart diseases can result in heart failure, which is a clinical syndrome that arises when the heart is unable to pump sufficient blood to meet the metabolic needs of the body at normal filling pressures (Alexander, Schlant, Fuster, O'Rourke, Roberts & Sonnenblick 1994). The goal of recording and visualizing cardiac data sets is to recognize and predict heart diseases.

The cardiac data set used in this paper is a finite element model of the human left ventricle developed by the Department of Physiology of the University of Auckland (Young, Kramer, Ferrari & ad Nathaniel Reichek 1994, Young, Imai, Chang & Axel 1994). The deformation of the *myocardium* (heart muscle) is represented by the *strain tensor*.

In this paper we use a visualization toolkit specifically designed for biomedical models (Wünsche 2002*b*, Wünsche 2002*a*) to visualize the strain tensor field and to evaluate the performance of a healthy and a diseased human left ventricle. The visualization techniques novel to this field are explained and the results are discussed and interpreted.

The first section of this paper gives an overview of cardiac diseases and explains why visualizing myocardial strain is important in their diagnosis and understanding. It follows an introduction of the FE model and the visualization toolkit used. The subsequent sections explain the visualization of the model and the efficient and easy derivation of performance measures from the finite element representation. We conclude with a discussion of our results and mention avenues for future research.

1.1 Notations

As shown in figure 1 (a) the heart consists of two main chambers, the left and the right ventricle. When discussing the heart it is convenient to introduce names for the different regions of the *myocardium* (heart muscle). Figure 1 (b) illustrates that the myocardium of the left ventricle is divided in circumferential direction into a *septal*, *anterior*, *lateral*, and *inferior* (or *posterior*) region. The anterior side of the left ventricle faces the chest, the inferior (posterior) side faces the back, and the septal region represents the inter-ventricular septum. In longitudinal direction the left ventricle is divided into an *apical*, a *mid-ventricular* or *equatorial*, and a *basal* region (Geskin, Kramer, Rogers, Theobald, Pakstis, Hu & Reichek 1998). Finally in radial direction the myocardium is divided into a *subendocardial*, *subepicardial*, and *mid-myocardial* region. The terms refer to the parts of the myocardium neighbouring the *epicardial surface* (the outer layer of the heart muscle), the *endocardial surface* (the layer lining the ventricular cavity), and the region between them, respectively.

The contraction of the heart is called *systole* and the expansion *diastole*. The moment of maximum contraction of the left ventricle is called (left-ventricular) *end-systole* and the moment of maximum expansion is called (left-ventricular) *end-diastole* (Young, Imai, Chang & Axel 1994).

2 Heart Failure

Causes of heart failure are differentiated into mechanical, myocardial, and rhythmic abnormalities (Alexander et al. 1994). Mechanical abnormalities include increased pressure or volume load (e.g., due to a dysfunctional valve) and bulging of the heart wall (ventricular aneurysm). Myocardial abnormalities includes metabolic disorders (e.g., diabetes), inflammation, and *ischemia* (blockage of the coronary artery). Abnormalities of the cardiac rhythm or conduction disturbances include standstill, irregular heart beat

---

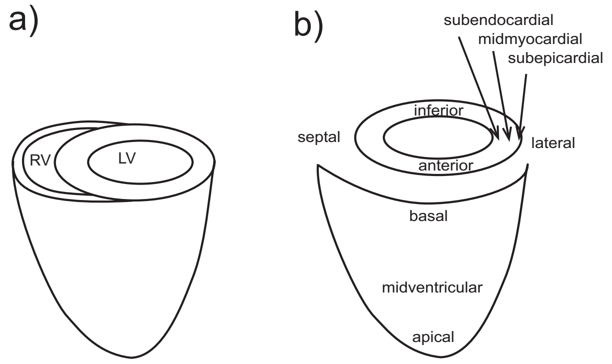

Figure 1: (a) Schematic drawing of the heart with the left (LV) and the right (RV) ventricle being indicated. (b) Illustration of the regions of the left-ventricular myocardium.

(*fibrillation*), and abnormally rapid heart beat (*tachycardia*).

The most common fatal heart disease is *myocardial infarction* (heart attack), which occurs when a coronary artery is completely blocked (*stenosis*) and an area of the heart muscle dies because it is completely deprived of oxygen for an extended period of time. Acute myocardial infarction starts in the subendocardium and spreads to the subepicardium within 20-40 minutes after occlusion of the coronary artery (Lim & Choi 1999). Permanently damaged muscle is replaced by scar tissue, which does not contract like healthy heart tissue, and sometimes becomes very thin and bulges during each heart beat (*aneurysm*) (Guttman, Zerhouni & McVeigh 1997, Alexander et al. 1994).

The analysis of myocardial function is important for the diagnosis of heart diseases, the planning of therapy (Lim & Choi 1999) and the understanding of the effect of cardiac drugs on regional function (Reichek 1999).

Many cardiac disorders result in regionally altered myocardial mechanics. Traditionally an abnormal contractile function of the ventricles has been determined by measuring the wall thickening using cine MRI images, Echocardiography (Myers, Stirling, Choy, Buda & Gallagher 1986, Alexander et al. 1994, Cheitlin, Alpert, Armstrong, Aurigemma, Beller, Bierman, Davidson, Davis, Douglas, Gillam, Lewis, Pearlman, Philbrick, Shah & Williams 1997, Antman, Bassand, Klein, Ohman, Sendon, Rydén, Simoons & Tendera 2000) and SPECT (Alexander et al. 1994). Reported wall thickening rates during systole for a healthy heart vary from 40% (Buvat, Bartlett, Kitsiou, Dilsizian & Bacharach 1997) to 80% (Holman, Buller, de Roos, van der Geest, Baur, van der Laarse, Bruschke, Reiber & van der Wall 1997). Detectable abnormalities include reduced wall thickening after myocardial infarction (Holman et al. 1997), regional wall thinning of an infarcted area and compensatory wall thickening and hypertrophy, and left ventricular enlargement (remodelling) (Alexander et al. 1994, pp.648).

Wall thickening, however, is only one indicator of impending heart failure and other motion dependent indicators have been reported in the literature (Willenheimer, Cline, Erhardt & Israelsson 1997, de Simone, Devereux, Koren, Mensah, Casale & Laragh 1996, Schussheim, Devereux, de Simone, Borer, Herrold & Laragh 1997, Guttman et al. 1997). A full description of the deformation behaviour of the myocardium is therefore desirable. Such a description is given by the strain tensor field **E** which is mathematical represented by a 3×3 matrix.

2.1 Myocardial Strain as an Indicator of Heart Failure

The concept of myocardial strain was originally introduced by Mirsky and Parmley (Mirsky & Parmley 1973). Strain is defined as the pure deformation (without translation and rotation). Scalar strain values can be derived from the strain tensor to quantify the length change of an infinitesimal material volume in a given direction (e.g., the circumferential or radial direction of the ventricle). Negative strain values are interpreted as a local shortening of the myocardium and positive strain values as a local elongation.

Abnormalities in the myocardial strain are detectable before first symptoms of a heart attack occur (Guttman et al. 1997) so that measuring and visualizing the strain might represent a useful diagnosis tool. Heimdal et al. report that the stress-strain relationship more selectively describes the overall tissue characteristics than the pressure-volume relationship (Heimdal, Stylen, Torp & Skjrpe 1998). McCulloch and Mazhari (McCulloch & Mazhari 2001) suggest several possible roles of strain and stress measurement in clinical diagnosis.

3 A Left-Ventricular Finite Element Model

Using *tagged Magnetic Resonance Imaging* (tagged MRI) the Department of Physiology of the University of Auckland has created a finite element model of the human left ventricle and the myocardial strain (Young, Kramer, Ferrari & ad Nathaniel Reichek 1994, Young, Kraitchman, Dougherty & Axel 1995). The following two subsections describe the definition of the finite element geometry and introduce the left-ventricular model used in this work.

3.1 Finite-Element Geometry

The geometry of a *finite element* model is described by a set of nodes and a set of elements, which have these nodes as vertices. The nodal coordinates are interpolated over an element using *interpolation functions*. Curvilinear elements can be defined by specifying nodal derivatives.

As an example of a finite element consider the cubic Hermite-linear Lagrange element in two dimensions shown in figure 2 (b). We first specify a parent element, shown in part (a) of the figure, which is a square in ξ-parameter space. The coordinates ξ_i $(0 \leq \xi_1, \xi_2 \leq 1)$ are called the element or *material coordinates*. The value of some variable u (e.g., temperature) at the material coordinates ξ is then specified by interpolating the variables u_i linearly in the given parameter direction. In our example we assume that additionally derivatives in ξ_1-direction $\left(\frac{\partial u}{\partial \xi_1}\right)_i$ $(i = 1, \ldots, 4)$ are specified at the element nodes. In this case a cubic Hermite interpolation is performed in that direction.

The cubic Hermite-linear interpolation of u over the entire 2D parameter space is then defined by the tensor products of the interpolation functions in each parameter direction:

$$\begin{aligned} & u(\xi_1, \xi_2) = \\ & H_1^0(\xi_1) L_1(\xi_2) u_1 + H_2^0(\xi_1) L_1(\xi_2) u_2 \\ + \quad & H_1^0(\xi_1) L_2(\xi_2) u_3 + H_2^0(\xi_1) L_2(\xi_2) u_4 \end{aligned} \tag{1}$$

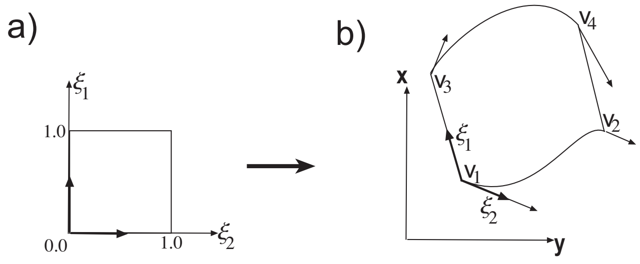

Figure 2: A cubic Hermite-linear Lagrange finite element.

$$
\begin{aligned}
&+\; H_1^1(\xi_1)L_1(\xi_2)\left(\frac{\partial u}{\partial \xi_1}\right)_1 + H_2^1(\xi_1)L_1(\xi_2)\left(\frac{\partial u}{\partial \xi_1}\right)_2\\
&+\; H_1^1(\xi_1)L_2(\xi_2)\left(\frac{\partial u}{\partial \xi_1}\right)_3 + H_2^1(\xi_1)L_2(\xi_2)\left(\frac{\partial u}{\partial \xi_1}\right)_4
\end{aligned}
$$

where

$$L_1(\xi) = 1 - \xi, \quad \text{and} \quad L_2(\xi) = \xi \tag{2}$$

are the one-dimensional linear Lagrange basis functions, and

$$
\begin{aligned}
H_1^0(\xi) &= 1 - 3\xi^2 + 2\xi^3, & H_1^1(\xi) &= \xi(\xi-1)^2\\
H_2^0(\xi) &= \xi^2(3 - 2\xi), & H_2^1(\xi) &= \xi^2(\xi-1)
\end{aligned}
\tag{3}
$$

are the one-dimensional cubic Hermite basis functions.

The geometry of an element in world coordinates (figure 2 (b)) is obtained by specifying the world-coordinates $\mathbf{v}_i$ and the ξ_1-tangents $\left(\frac{\partial \mathbf{v}}{\partial \xi_1}\right)_i$ $(i = 1, \ldots, 4)$ of the element vertices and interpolating them as above.

3.2 The Model of the Left Ventricle

The geometry of the left-ventricle, shown in figure 3, is described by 16 finite elements and uses bicubic Hermite interpolation in circumferential and longitudinal directions with linear interpolation in radial direction (Young, Kramer, Ferrari & ad Nathaniel Reichek 1994, Young et al. 1995).

The authors obtain the ventricular geometry by tracing ventricular contours on MRI slices and by fitting the FE mesh to it.

Strain information is obtained from tagged MRI images as shown in figure 4. When the heart deforms the tag lines deform with it making it possible to compute the displacement field of the myocardium from which the strain tensor is derived (Young, Imai, Chang & Axel 1994). The strain field is defined as a regular grid of $10 \times 10 \times 6$ sample points over the material coordinates of the tensor. The strain tensors themselves are defined with respect to the material coordinate system of the corresponding elements.

In the following discussion we evaluate and visualize two models of the left ventricle. The first model, shown in figure 3, represents a healthy left ventricle. The second model is from a heart diagnosed with non-ischemic *dilated cardiomyopathy*, which is characterized by cardiac enlargement, increased cardiac volume, reduced ejection fraction, and congestive failure (Young, Dokos, Powell, Sturm, McCulloch, Starling, McCarthy & White 2000).

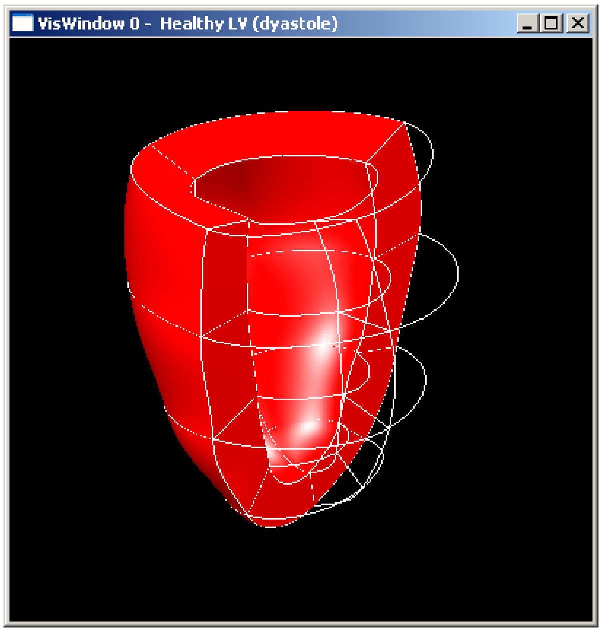

Figure 3: Finite Element Model of a healthy left ventricle.

4 Computing Ventricular Performance Measures

The performance of the left ventricle is often specified using various length, surface and volume measures such as its systolic and diastolic volume and its ejection fraction. Using our visualization toolkit the user can specify elements, faces and parameter curves and compute their volume, area and length, respectively.

4.1 Computing Volume Measures

The volume of a single element is obtained by integrating the identity function over the finite element in world coordinates. The calculation is simplified by using the substitution rule of multi-dimensional integration (Heuser 1981, p.478)

$$\int_{\mathbf{g}(\Omega)} f(\mathbf{x})\, d\mathbf{x} = \int_{\Omega} f(\mathbf{g}(\xi))|det\mathbf{J}_{\mathbf{g}}(\xi)|\, d\xi \tag{4}$$

where f is the identity function, Ω is the unit cube representing the domain of the parent element, $\mathbf{g}$ is the transformation function from ξ-coordinates to world coordinates and $\mathbf{J}_{\mathbf{g}}$ is its Jacobian. The resulting integral can be evaluated efficiently using Gaussian Quadrature (Burnett 1987). Determining the degree of each ξ-coordinate in the polynomial expression inside the integral shows that 5 gauss points in ξ_1 and ξ_2 direction and 2 gauss points in ξ_3 direction are sufficient to achieve exact integration.

	ED	ES	Volume reduction
Healthy heart	217.5	159.1	26.85%
Sick heart	336.7	305.3	9.32%

Table 1: Myocardial volume (in cm^3) of the healthy and the sick heart at end-diastole (ED) and end-systole (ES).

Table 1 shows the volume of the heart muscle at end-diastole and end-systole and the resulting vol-

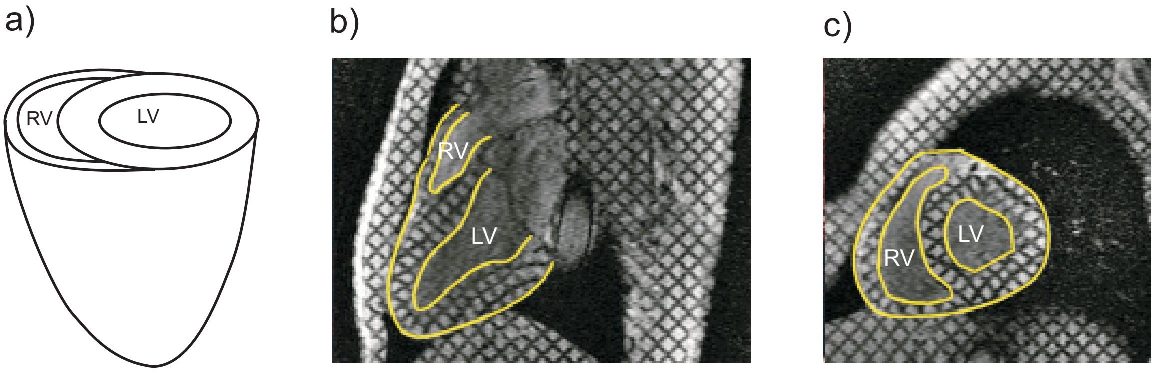

Figure 4: Schematic drawing (a) and a long axis (b) and short axis (c) tagged MRI image of the heart. All three images show the left ventricle (LV), the right ventricle (RV) and the endocardial surface and epicardial surface (in yellow) of the heart.

ume reduction during contraction. In general the myocardium is considered incompressible but Denney and Prince estimate that small volume changes up to 10% occur due to myocardial perfusion (Denney Jr. & Prince 1995). Our results show considerable higher values for the healthy heart which requires further investigation.

One of the most important measures of cardiac performance is the ventricular (blood) volume and the fraction of blood ejected during contraction. In order to apply the volume computation introduced above the left-ventricular cavity must be modeled by finite elements. Using our toolkit we can define centroids for any four vertices on the endocardial surface with common longitudinal ξ-coordinate. Connecting these vertices to the corresponding points on the endocardial surface results in 16 finite elements for the left ventricular cavity.

Figure 5 and 6 show the finite element models of the ventricular cavity of the healthy and sick heart at end-diastole and end-systole.

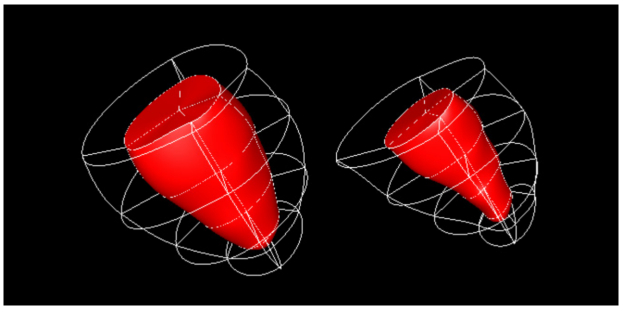

Figure 5: Ventricular cavities of the healthy heart at end-diastole (left) and end-systole (right).

Using equation 4 we can now compute the left ventricular volumes at end-diastole (ED) and end-systole (ES). The difference of these values represents the stroke volume [volume of ejected blood] (SV) and the ratio of stroke volume to the volume at end-diastole represents the ejection fraction (EF). The results for the healthy and diseased heart are shown in table 2.

The ventricular volume of the healthy heart at end-diastole is about $87cm^3$ and the stroke volume is $52cm^3$ resulting in an ejection fraction of about 60%. These values correspond well with data reported in the medical literature (Boxt 1999). For the diseased heart a considerable larger end-diastolic volume is observed. However, the stroke volume is only $36.23cm^3$ and about 30% smaller than for the healthy heart. The ejection fraction is only 11.5%. These values indicate a severe impairment of myocardial function.

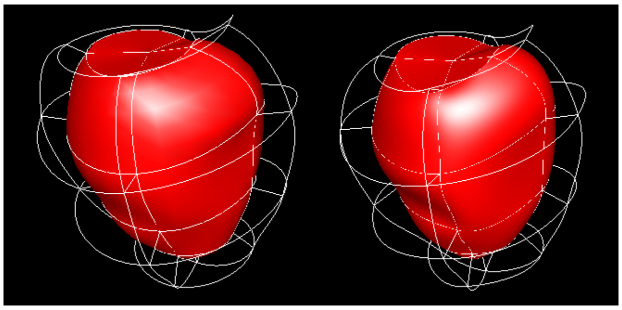

Figure 6: Ventricular cavities of the sick heart at end-diastole (left) and end-systole (right).

	ED	ES	SV	EF
Healthy heart	87.15	35.08	52.07	59.75%
Failing heart	314.18	277.94	36.23	11.53%

Table 2: Ventricular volume (in cm^3) of the healthy and diseased left ventricle at end-diastole (ED) and end-systole (ES), stroke volume (SV), and ejection fraction (EF).

4.2 Computing Ventricular Surface Areas

The area of a surface $\mathbf{\Phi} = \mathbf{\Phi}(u,v)$ over a parameter region K is computed by (Heuser 1981, p.505)

$$I(\Phi) = \int_K \left| \frac{\partial \mathbf{\Phi}}{\partial u} \times \frac{\partial \mathbf{\Phi}}{\partial v} \right| d(u,v) =$$

$$\int_K \sqrt{ \left| \begin{array}{cc} \frac{\partial \Phi_2}{\partial u} & \frac{\partial \Phi_2}{\partial v} \\ \frac{\partial \Phi_3}{\partial u} & \frac{\partial \Phi_3}{\partial v} \end{array} \right|^2 + \left| \begin{array}{cc} \frac{\partial \Phi_3}{\partial u} & \frac{\partial \Phi_3}{\partial v} \\ \frac{\partial \Phi_1}{\partial u} & \frac{\partial \Phi_1}{\partial v} \end{array} \right|^2 + \left| \begin{array}{cc} \frac{\partial \Phi_1}{\partial u} & \frac{\partial \Phi_1}{\partial v} \\ \frac{\partial \Phi_2}{\partial u} & \frac{\partial \Phi_2}{\partial v} \end{array} \right|^2 } \, d(u,v)$$

We are only interested in surfaces parallel to one of the material coordinate axes. For example, the endocardial surface is given by the coordinate planes in material space with $\xi_3 = 0$. In this case $\mathbf{\Phi}(\xi_1, \xi_2) = \mathbf{x}(\mathbf{f}(\xi_1, \xi_2))$ where $\mathbf{f}(\xi_1, \xi_2) = (\xi_1, \xi_2, 0)$ and

$$\frac{\partial \mathbf{\Phi}}{\partial \xi_1} = \frac{\partial \mathbf{x}}{\partial f_1}\frac{\partial f_1}{\partial \xi_1} + \frac{\partial \mathbf{x}}{\partial f_2}\frac{\partial f_2}{\partial \xi_1} + \frac{\partial \mathbf{x}}{\partial f_3}\frac{\partial f_3}{\partial \xi_1} = \frac{\partial \mathbf{x}}{\partial f_1} = \frac{\partial \mathbf{x}}{\partial \xi_1}$$

and similarly for the other partial derivatives. The surface area A is therefore given by

$$A = I(\Phi) =$$

$$\int_0^1\int_0^1 \sqrt{ \begin{vmatrix} \frac{\partial x_2}{\partial \xi_1} & \frac{\partial x_2}{\partial \xi_2} \\ \frac{\partial x_3}{\partial \xi_1} & \frac{\partial x_3}{\partial \xi_2} \end{vmatrix}^2 + \begin{vmatrix} \frac{\partial x_3}{\partial \xi_1} & \frac{\partial x_3}{\partial \xi_2} \\ \frac{\partial x_1}{\partial \xi_1} & \frac{\partial x_1}{\partial \xi_2} \end{vmatrix}^2 + \begin{vmatrix} \frac{\partial x_1}{\partial \xi_1} & \frac{\partial x_1}{\partial \xi_2} \\ \frac{\partial x_2}{\partial \xi_1} & \frac{\partial x_2}{\partial \xi_2} \end{vmatrix}^2 }\, d\xi_1 d\xi_2$$

where the partial derivatives $\frac{\partial x_i}{\partial \xi_j}$ are the entries of the Jacobian $J_{\mathbf{g}}$ of the coordinate transformation function. The integral is again evaluated by gauss integration. Simulations showed that even though the integrand is not polynomial the gauss integration gives five figure accuracy (Wünsche 2002*b*).

	ED	ES	Area reduction
Healthy Epi	201.7	147.7	26.75 %
Healthy Endo	93.4	53.4	42.76 %
Sick Epi	350.6	324.6	7.40 %
Sick Endo	218.7	200.0	8.55 %

Table 3: Surface area (in cm^2) of the endocardial (endo) and the epicardial (epi) surface of the healthy and sick left ventricle at end-diastole (ED) and end-systole (ES).

Table 3 shows the surface areas of the endocardial and the epicardial surface. It can be seen that the area reduction of the sick left ventricle is severely impaired. Since the muscle fibers of the myocardium are aligned with these surfaces the measurements indicate that either muscle fiber don't contract (e.g., due to fibrosis) or that they contract in some regions but expand in other region of the surface. In order to further examine this deformation behaviour we will visualize the strain tensor in section 6.

Using the above technique it is also possible to compute the midventricular cavity cross-sectional area. We get as results $13.27cm^2$ at end-diastole and $5.81cm^2$ at end-systole. From these values we determine a mid ventricular radius of $2.06cm$ at end-diastole and $1.36cm$ at end-systole.

4.3 Computing Length Measures

Similar to the volume and area computations it is also possible to compute the arc-length of a parametric function $\gamma : [a,b] \rightarrow \mathbb{R}^p$ (Heuser 1981, p.354)

$$L(\boldsymbol{\gamma}) = \int_a^b |\dot{\boldsymbol{\gamma}}(t)|dt = \int_a^b \sqrt{\dot{\gamma_1}^2 + \ldots + \dot{\gamma_p}^2}dt$$

Assume the start point and end point of a parameter curve within a finite element are ξ_s and ξ_e. Then the curve in material coordinates is the linear line segment $\boldsymbol{\gamma}(t) = \boldsymbol{\xi}^s + t(\boldsymbol{\xi}^e - \boldsymbol{\xi}^s)$ with $t \in [0,1] = [a,b]$ so that

$$\dot{\boldsymbol{\gamma}}(t) = J_{\mathbf{g}}(\mathbf{t})(\gamma^e - \gamma^s)$$

where $\mathbf{g}$ is again the transformation function from ξ-coordinates to world coordinates and J is its Jacobian.

Using this measure it is possible to compute the length of a circumflex arc of a ventricle by the length of a curve on the endocardial surface with a constant longitudinal ξ-parameter. The length of this curve can then be used to derive a value for the ventricular radius at that position. However, reliable results are only obtained if the arc is approximately planar and orthogonal to the long axis of the ventricle. While the technique could also be used to approximate the wall thickness at a point it does not necessarily yield the shortest distant between the endocardial and epicardial surface. Better computational techniques are suggested in (van der Geest & Reiber 1999).

5 A Visualization Toolkit

The following section examines the deformation of the heart by using 3D visualizations. All visualizations are created using a toolkit we designed for biomedical datasets and models (Wünsche 2002*b*). The toolkit, shown in figure 7, was programmed in C/C++ and uses OpenGL, GLU, GLUT and FLTK, a LGPL'd C++ graphical user interface toolkit for X (UNIX), OpenGL, and WIN32 (Spitzak n.d.).

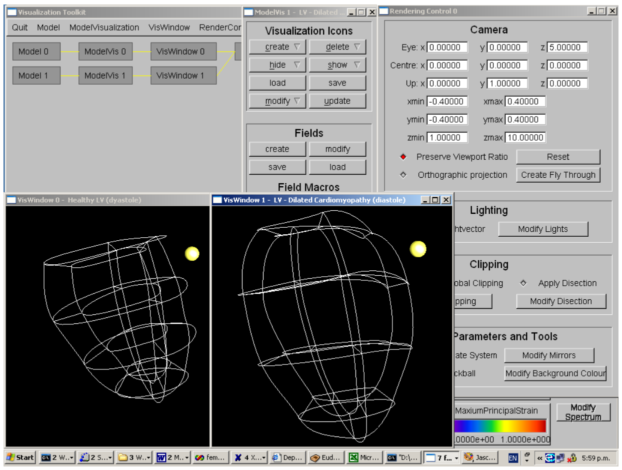

Eye: x 0.00000 y 0.00000 z 5.00000
Centre: x 0.00000 y 0.00000 z 0.00000
Up: x 0.00000 y 1.00000 z 0.00000
xmin -0.40000 xmax 0.40000
ymin -0.40000 ymax 0.40000
zmin 1.00000 zmax 10.00000
● Preserve Viewport Ratio
○ Orthographic projection

Figure 7: A screen shot of the visualization toolkit. The yellow spheres indicate the septal wall.

Three features of our toolkit are worth mentioning. The first feature is a modular object-oriented (OO) design with separate objects describing input data sets, visualization icons, rendering parameters, and visualization windows. A visualization is achieved by defining relationships, subject to some constraints, between these objects. The design facilitates the definition of simultaneous visualizations of multiple models such as the simultaneous display of a sick and a healthy heart. Using the same rendering parameters ensures that both models are displayed using the same view, scaling, orientation and lighting. Similarly the same model can be displayed in multiple windows making it possible, for example, to use simultaneously a global and a local view.

The second feature is a generalised field data structure that allows the user to mix data sets from different sources such as finite element data, MR or PET raw data and analytical data in the form of algebraic functions. Finite element data can be represented in material and world coordinates and new fields can be interactively derived using a simple to use graphical user interface. Figure 8 shows the graphical user interfaces for constructing new fields (left) and for defining macros for commonly used derived fields (right).

Finally our toolkit contains a variety of visualization techniques which can be applied to the data set using various element and point selection tools. A global colour map control makes it possible that icons for different visualizations use the same colour maps which makes it easier for the user to compare multiple models. Defining new colour maps is often necessary

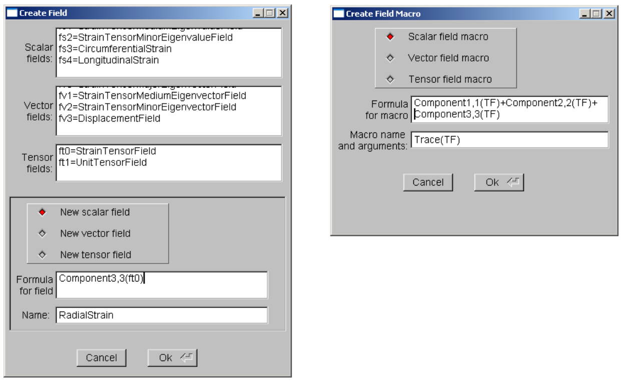

Scalar fields:
fs2=StrainTensorMinorEigenvalueField
fs3=CircumferentialStrain
fs4=LongitudinalStrain

Vector fields:
fv1=StrainTensorMediumEigenvectorField
fv2=StrainTensorMinorEigenvectorField
fv3=DisplacementField

Tensor fields:
ft0=StrainTensorField
ft1=UnitTensorField

● New scalar field
○ New vector field
○ New tensor field

Formula for field: Component3,3(ft0)

Name: RadialStrain

● Scalar field macro
○ Vector field macro
○ Tensor field macro

Formula for macro: Component1,1(TF)+Component2,2(TF)+Component3,3(TF)

Macro name and arguments: Trace(TF)

Figure 8: Graphical user interfaces for creating new fields from arithmetic expressions (left) and for creating macros (right).

to avoid colour clashes when displaying various visualization icons simultaneously and gives the user additional freedom when exploring the data set. A colour map can be modified to be exponential (colour spectrum is reparameterized with an exponential function) or cyclical (colour map consists of multiple cycles of the colour spectrum). An exponential colour map improves qualitative perception of values when using predominantly equal-valued fields with small regions of extreme values. Cyclical colour maps have the advantage of giving gradient information without inducing visual cluttering. They are therefore useful when examining symmetry patterns and discontinuities in a scalar field (Wünsche & Lobb 2001).

6 The Visualization of Myocardial Strain

The measurements presented so far indicated a severe impairment of the contraction of the sick heart. In order to better understand the local deformation of the myocardium more information is required. This section presents and explains various visualizations of the strain tensor and of quantities derived from it.

Most visualization methods in this section use the property that for any 3-dimensional symmetric tensor $\mathbf{T}$ there always exist 3 *eigenvalues* λ_i and 3 mutually perpendicular *eigenvectors* $\mathbf{v}_i$ such that

$$\mathbf{T}\mathbf{v}_i = \lambda_i \mathbf{v}_i \quad i = 1, 2, 3 \tag{5}$$

The eigenvalues and eigenvectors define the tensor completely. Since the strain tensor $\mathbf{E}$ is symmetric (Lai, Rubin & Krempl 1986) equation 5 applies. The eigenvectors $\mathbf{v}_1$, $\mathbf{v}_2$, and $\mathbf{v}_3$ of $\mathbf{E}$ are the *principal directions* of the strain, i.e., the directions where there is no shear strain. The eigenvalues λ_1, λ_2, and λ_3 are the *principal strains* and give the unit elongations in the principal directions. The maximum, medium, and minimum eigenvalue are called the *maximum*, *medium*, and *minimum principal strain*, respectively.

As an initial visualization we display tensor ellipsoids at regular sample point throughout the mid-myocardium. Tensor ellipsoids encode the principal directions and strains by the directions and lengths, respectively, of the axes of the ellipsoid. In order to encode the sign of an eigenvalue we divide an ellipsoid into six segments using a hexagonal subdivision of the unit sphere. A red segment indicates expansion and a blue segment indicates contraction. Note that the 3D geometry is difficult to perceive from a static image. Rotating the model enables the brain to differentiate ellipsoids in the foreground and background. Consequently our toolkit incorporates a function to animate the trackball which is used to rotate the model.

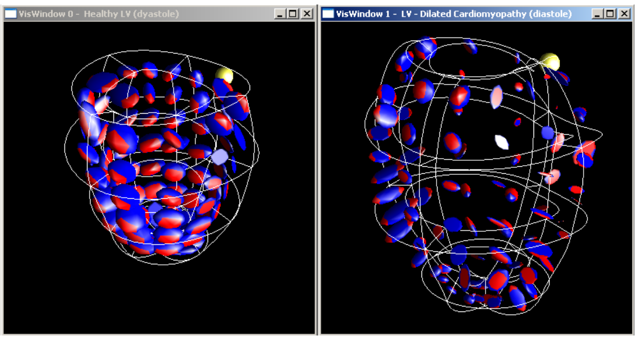

Figure 9: The strain field in the midwall of the healthy (left) and diseased (right) left ventricle visualized using tensor ellipsoids. The septal wall is indicated by a yellow sphere.

Figure 9 shows that for the healthy ventricle the myocardium expands in the radial direction (wall thickening) and contracts in the longitudinal and circumferential direction with the circumferential contraction being in general larger. The contraction is smallest in the septum and largest in the free wall. The results correspond well with measurements reported in the literature (Lugo-Olivieri, C.Moore, Poon, Lima, McVeigh & Zerhouni 1994, Guttman et al. 1997, Young, Imai, Chang & Axel 1994, Denney Jr. & McVeigh 1997).

The deformation of the sick ventricle is highly abnormal. Whereas the anterior-lateral wall of the ventricle displays an almost normal deformation behaviour, albeit with smaller strain values, the situation is the exact opposite in the septal wall of the ventricle. Here the myocardium is contracting in the radial direction and is expanding in the circumferential and longitudinal direction.

While tensor ellipsoids contain the complete tensor information the resulting visualization suffers from visual cluttering. Furthermore information is only displayed at selected sample points. A one-dimensional continuous representation of the strain tensor is achieved using hyperstreamlines (Delmarcelle & Hesselink 1993).

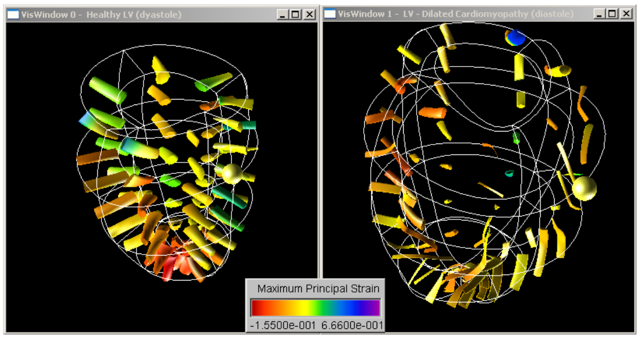

Figure 10: The strain field in the midwall of the healthy (left) and the diseased (right) left ventricle visualized using hyperstreamlines in the direction of the major principal strains. The septal wall is indicated by a yellow sphere.

The trajectory of a hyperstreamline is a streamline in the eigenvector field, i.e., the trajectory is ob-

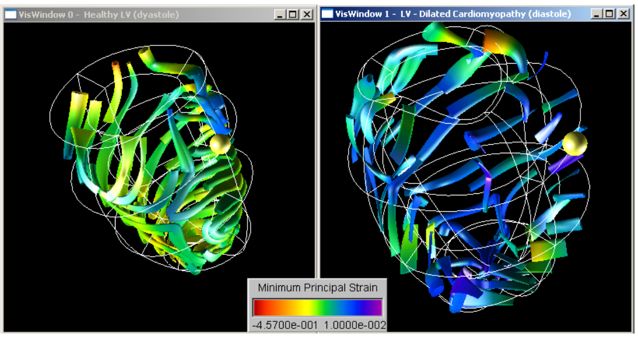

Figure 11: The strain field in the midwall of the healthy (left) and the diseased (right) left ventricle visualized using hyperstreamlines in the direction of the minor principal strains. The septal wall is indicated by a yellow sphere.

tained by starting at a point and integrating in the direction of the selected eigenvector. The other two eigenvectors and corresponding eigenvalues define the axes and lengths of the ellipsoidal cross section of the hyperstreamline. The remaining eigenvalue is colour mapped onto the hyperstreamline.

Figure 10 and 11 show hyperstreamlines in the direction of the major and minor principal strain, respectively.

The images show clearly that for the healthy heart the major principal strain is positive (see colour scale) and oriented in radial direction throughout the myocardial wall. Furthermore it can be seen from the diameter of the cross section of the hyperstreamline that with the exception of the septal wall the magnitude of the transverse strains increases from the epicardial to the endocardial surface. We are not aware of any previous work showing all these properties with a single image.

The minimum principal strain of the healthy left ventricle is compressive throughout most of the myocardium and its direction resembles over most of the myocardium a spiral moving towards the apex. This strain direction corresponds well with the motion of the heart described in the medical literature: The septum performs initially an anticlockwise rotation (apex-base view) but later a more radial movement. The apex rotates overall anticlockwise whereas the base rotates clockwise. The anterioseptal regions of the mid and apical levels and the posterioseptal region of the base perform a hook-like motion because of a reversal of rotation (Young, Imai, Chang & Axel 1994). Note that we have in the inferior-septal region an interesting feature where the hyperstreamlines change suddenly their direction.

This feature can be examined in more detail using a line integral convolution texture. Line Integral Convolution (LIC) was originally proposed by Cabral and Leedom as a method to visualize vector fields by convolving a noise texture with the field (Cabral & Leedom 1993). We use the direction of the minor principal strain as a vector field and use its magnitude to colour map the texture. Additional details are found in (Wünsche 2002*b*).

Figure 12 shows that the maximum compressive strain in the midmyocardium is predominantly oriented in circumferential direction with a slight downward tilt. Several interesting points exists where the strain suddenly changes direction. Results from tensor analysis show that these points are *degenerate points* for which at least two eigenvalue are equal (Delmarcelle & Hesselink 1994). An example of such a point is indicated by the white rectangle and is shown enlarged on the right hand side of the image. We found that most of the degenerate points occur on or near the septal wall. The unusual variations in strain orientation might be caused by the right ventricular wall which is connected to the left ventricular wall at both sides of the septum. In contrast the strain field of the sick heart contains considerable more degenerate points distributed throughout the myocardium.

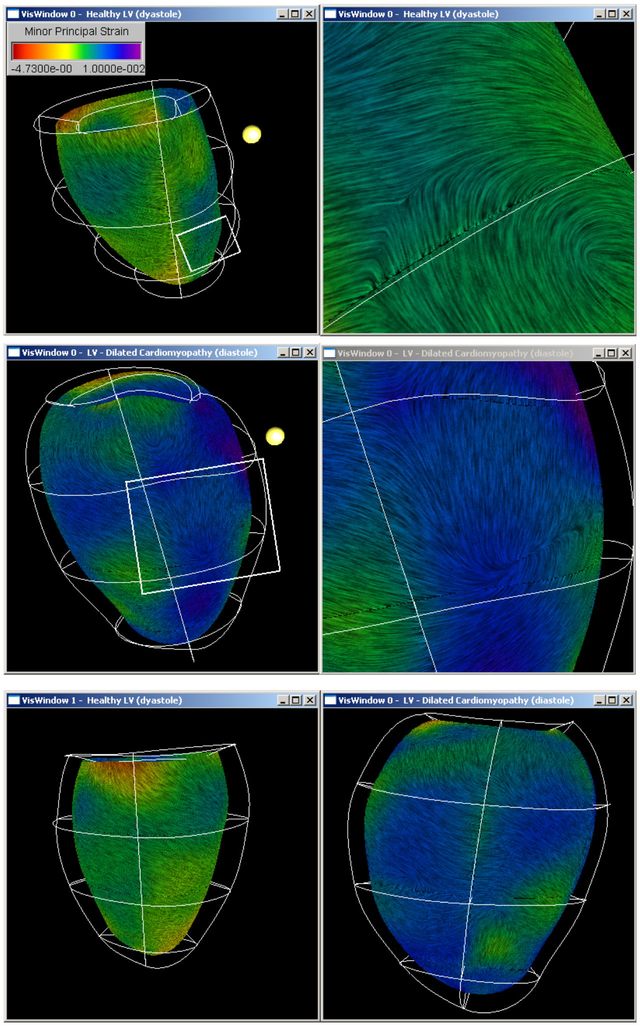

Figure 12: The minor principal strain (maximum contracting strain) of the healthy (top) and sick (middle) heart visualized using Line Integral Convolution. The bottom images show the lateral wall of the healthy (left) and sick (right) heart.

We conclude this section with an examination of the distribution of the strains in the material directions. Since the strain tensor is defined with respect to the material coordinates the strains in circumferential, longitudinal and radial direction are given by the normal components E_{11}, E_{22} and E_{33}, respectively, of the strain tensor $\mathbf{E}$.

Figure 13 visualizes the normal strains on the endocardial surface using colour mapping and shows additionally the 0-isosurface, which separates contracting and expanding regions.

The images on the left of the figures show clearly that the healthy left ventricle contracts in circumferential and longitudinal direction and expands in radial direction. The only exceptions are some parts of the model boundary and, for the radial strain, three small cylindrical regions at the apex and the septal

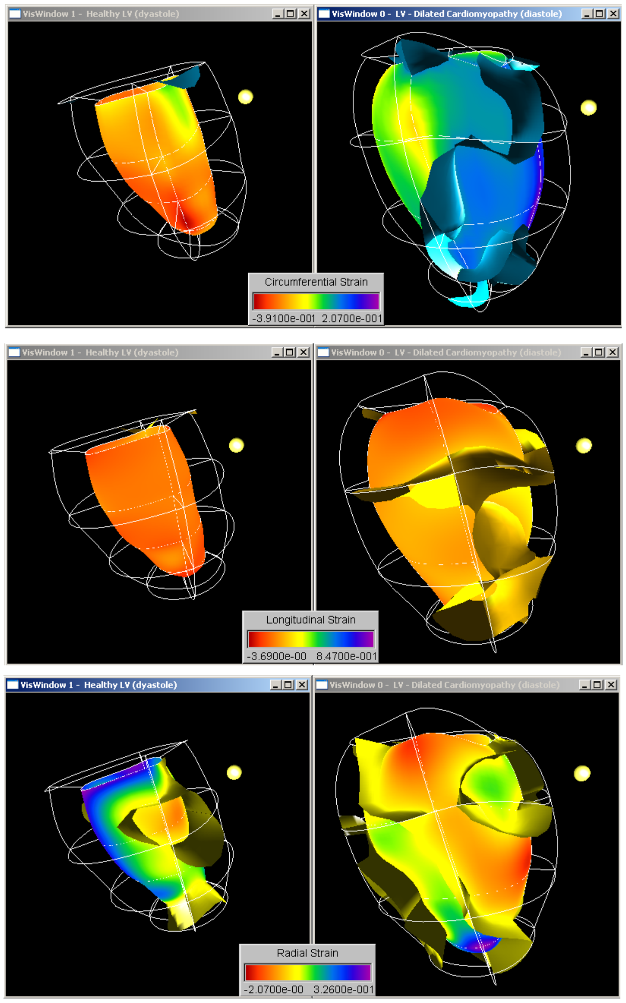

Figure 13: The normal strain in circumferential (top), longitudinal (middle) and radial (bottom) direction on the endocardial surface of the healthy (left) and sick (right) heart. The images show also the 0-isosurface which separates region of contractile and expanding strain. The septal wall is indicated by a yellow sphere.

and lateral wall. All three normal strain components are distributed relatively evenly over the endocardial surface.

For the diseased heart the lateral wall and part of the anterior and inferior wall contract in circumferential and longitudinal direction. Wall thickening is observed in the basal-lateral wall, the basal-septal wall and in parts of the anterior and inferior wall. The rest of the myocardium shows an abnormal deformation. As a result of the strain distribution the ventricle does not contract evenly but rather performs a shape change.

We are also interested in the shear components of the strain tensor. It is known that during contraction the heart changes predominantly in diameter. LeGrice et al. (LeGrice, Takayama & Covell 1995) reports 8% lateral expansion but 40% wall thickening. This indicates reorganization of the myocytes during systole. Because of the sheet structure of the myocardium it has been proposed that the sheets can slide over another restricted mainly by the length of the interconnecting collagen fibers (LeGrice et al. 1995). The shear properties of the myocardium resulting from this sliding motion are characterized in (Dokos, LeGrice, Smaill, Kar & Young 2000, Dokos, Smail, Young & LeGrice 2002). The shear is most restricted in the direction of the sheet normals and the maximum shear is possible in the fiber direction. Wall shear is thought to be an important mechanism of wall thickening during systole and therefore may play a substantial role in the ejection of blood from the ventricle.

Figure 14 shows the shear in the circumferential-longitudinal plane. For the healthy heart the shear strain is positive for most of the myocardium with the exception of some subepicardial regions close to the merging point with the right ventricular wall. No consistent behaviour can be found for the diseased heart. The shear in the lateral wall resembles most closely the normal range of values whereas the anterior-basal region exhibits extremely high negative strains, which might indicate impending tissue damage.

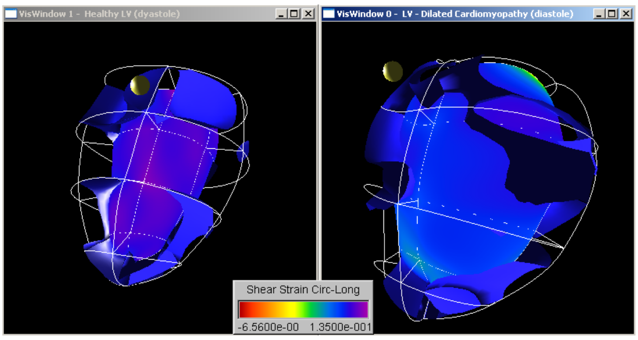

Figure 14: The circumferential-longitudinal shear strain component in the healthy (left) and sick (right) heart visualized using a colour map and the 0-isosurface. The septal wall is indicated by a yellow sphere.

7 Conclusion

Visualizing the strain field improves the understanding of the complex deformation of the heart muscle. Using techniques new to the biomedical field offers additional insight. The visual information can be supplemented by computing ventricular performance measures which are easily obtained from the finite element model using numerical integration.

The visualization of the healthy heart confirms observations previously reported in the literature. Using tensor ellipsoids and hyperstreamlines makes it possible to visualize complex deformation behaviour in a single image. Line integral convolution uncovered the presence of degenerate points at which the principal strains suddenly change direction. Further investigations are necessary to find the relationship between degenerate points, fiber structure, and the ventricular anatomy. Furthermore we want to explore their significance (if any) for diagnosing abnormalities in the heart motion.

Visualizing a ventricle with dilated cardiomyopathy showed that the deformation of the lateral wall resembles most closely the expected motion whereas the septal wall behaved almost contrary to the expected deformation. Very large negative shear strains were recorded in the anterior-basal wall of the ventricle. The combined effect of these deformations seems to be a pumping action by shape deformation (from circular to ellipsoidal cross section) rather then by contraction.

The visualizations and measurement performed in this paper demonstrated the usefulness of our visualization toolkit for exploring biomedical models. Using the unique field data structure enables the interactive definition of new measures and facilitates the exploration of the data set. The modular OO-design allows comparison of multiple models, which is further enhanced by the user interface for colour map design and control. The toolkit provides many standard visualization techniques in use today with some improvements being implemented by us.

8 Future Research

We are interested in visualizing other data sets of diseased hearts, in particularly models of ischemic myocardium. It is known that small changes in the deformation behaviour of the myocardium occur before first symptoms of a cardiac infarct develop and we hope that visualizing myocardial strain supports the detection of regions of low blood perfusion. Non-traditional visualization methods such as hyperstreamlines, LIC and tensor topology (Delmarcelle & Hesselink 1994, Lavin, Levy & Hesselink 1997) seem to be particularly promising for this purpose.

Of particular interest is the relationship between myocardial strain and fiber structure. Recent research suggests that measurement of the in vivo fiber structure is possible using diffusion tensor imaging (Mori, Xue, Crain, Solaiyappan, Chacko & v. Zijl n.d.). Further information could be provided by fusing our data with functional data obtained by PET and SPECT (Ruddy, deKamp & Beanlands 1999).

9 Acknowledgments

We would like to thank Alistair A. Young from the Department of Physiology of the University of Auckland, Auckland, New Zealand, for valuable discussions and for providing us with the models of the left ventricle. Our thanks also goes to Dr. Richard White of the Cleveland Clinic, Cleveland, Ohio, USA, who kindly provided tagged MRI data of a left ventricle diagnosed with dilated cardiomyopathy.

References

Alexander, R. W., Schlant, R. C., Fuster, V., O'Rourke, R. A., Roberts, R. & Sonnenblick, E. H., eds (1994), *Hurst's The Heart*, 9 edn, McGraw-Hill Companies, Inc., London.

Antman, E., Bassand, J.-P., Klein, W., Ohman, M., Sendon, J. L. L., Rydén, L., Simoons, M. & Tendera, M. (2000), 'Myocardial infarction redefined – a consensus document of the joint european society of cardiology/american college of cardiology committee for the redefinition of myocardial infarction', *Journal of the American College of Cardiology* **36**(3), 959–969.

Boxt, L. M. (1999), 'From the RSNA refresher courses: Cardiac MR imaging: A guide for the beginner', *Radiographics* **19**(4), 1009 – 1025. URL: `http://radiographics.rsnajnls.org/content/vol19/issue4/`.

Burnett, D. S. (1987), *Finite Element Analysis - From Concepts to Applications*, Addison-Wesley Publication Company Inc.

Buvat, I., Bartlett, M. L., Kitsiou, A. N., Dilsizian, V. & Bacharach, S. L. (1997), 'A "hybrid" method for measuring myocardial wall thickening from gated PET/SPECT images', *The Journal of Nuclear Medicine* **38**(2), 324–329.

Cabral, B. & Leedom, L. C. (1993), Imaging vector fields using line integral convolution, *in* J. T. Kajiya, ed., 'Computer Graphics (SIGGRAPH '93 Proceedings)', Vol. 27, ACM SIGGRAPH, Addison Wesley, pp. 263–272.

Cheitlin, M. D., Alpert, J. S., Armstrong, W. F., Aurigemma, G. P., Beller, G. A., Bierman, F. Z., Davidson, T. W., Davis, J. L., Douglas, P. S., Gillam, L. D., Lewis, R. P., Pearlman, A. S., Philbrick, J. T., Shah, P. M. & Williams, R. G. (1997), 'ACC/AHA guidelines for the clinical application of echocardiography: a report of the american college of cardiology/american heart association task force on practice guidelines (committee on clinical application of echocardiography)', *Journal of the American College of Cardiology (JACC)* **29**(4), 862 – 879.

de Simone, G., Devereux, R. B., Koren, M. J., Mensah, G. A., Casale, P. N. & Laragh, J. H. (1996), 'Midwall left ventricular mechanics: an independent predictor of cardiovascular risk in arterial hypertension', *Circulation* **93**(2), 259 – 265.

Delmarcelle, T. & Hesselink, L. (1993), 'Visualizing second-order tensor fields with hyperstreamlines', *IEEE Computer Graphics and Applications* **13**(4), 25 – 33.

Delmarcelle, T. & Hesselink, L. (1994), The topology of symmetric, second-order tensor fields, *in* R. D. Bergeron & A. E. Kaufman, eds, 'Proceedings of Visualization '94', IEEE, pp. 140 – 148.

Denney Jr., T. S. & McVeigh, E. R. (1997), 'Model-free reconstruction of three-dimensional myocardial strain from planar tagged MR images', *Journal of Magnetic Resonance Imaging* **7**(5), 799 – 810.

Denney Jr., T. S. & Prince, J. L. (1995), 'Reconstruction of 3-D left ventricular motion from planar tagged cardiac MR images: An estimation theoretic approach', *IEEE Transactions on Medical Imaging* **14**(4), 625 – 635.

Dokos, S., LeGrice, I. J., Smaill, B. H., Kar, J. & Young, A. A. (2000), 'A triaxial-measurement shear-test device for soft biological tissue', *Journal of Biomechanical Engineering* **122**(5), 471–478.

Dokos, S., Smail, B. H., Young, A. A. & LeGrice, I. J. (2002), 'Shear properties of passive ventricular myocardium', *American Journal of Physiology* **283**(6), H2650–H2659.

Geskin, G., Kramer, C. M., Rogers, W. J., Theobald, T. M., Pakstis, D., Hu, Y.-L. & Reichek, N. (1998), 'Quantitative assessment of myocardial viability after infarction by dobutamine magnetic resonance tagging', *Circulation* **98**(3), 217 – 223.

Guttman, M. A., Zerhouni, E. A. & McVeigh, E. R. (1997), 'Analysis of cardiac function from MR images', *IEEE Computer Graphics and Applications* **7**(2), 30 – 38.

Heimdal, A., Stylen, A., Torp, H. & Skjrpe, T. (1998), 'Real-time strain rate imaging of the left ventricle by ultrasound', *Journal of the American Society of Echocardiography* **11**, 1013 – 1019. URL:

http://www.stud.ntnu.no/~heimdal/SRI/RealTime.

Heuser, H. (1981), *Lehrbuch der Analysis*, Vol. 2, B.G. Teubner.

Holman, E. R., Buller, V. G. M., de Roos, A., van der Geest, R. J., Baur, L. H. B., van der Laarse, A., Bruschke, A. V. G., Reiber, J. H. C. & van der Wall, E. E. (1997), 'Detection and quantification of dysfunctional myocardium by magnetic resonance imaging: A new three-dimensional method for quantitative wall-thickening analysis', *Circulation* **95**(4), 924–931.

Lai, W. M., Rubin, D. & Krempl, E. (1986), *Introduction to Continuum Mechanics*, Vol. 17 of *Pergamon Unified Engineering Series*, revised edition in SI/metric units edn, Pergamon Press, Headington Hill Hall, Oxford OX3 0BW, England.

Lavin, Y., Levy, Y. & Hesselink, L. (1997), Singularities in nonuniform tensor fields, *in* R. Yagel & H. Hagen, eds, 'Proceedings of Visualization '97', IEEE, pp. 59 – 66.

LeGrice, I. J., Takayama, Y. & Covell, J. W. (1995), 'Transverse shear along myocardial cleavage planes provides a mechanism for normal systolic wall thickening', *Circulation Research* **77**(1), 182–193.

Lim, T.-H. & Choi, S. I. (1999), 'MRI of myocardial infarction', *Journal of Magnetic Resonance Imaging* **10**(5), 686 – 693. Special Issue: Cardiovascular MRI.

Lugo-Olivieri, C. H., C.Moore, C., Poon, E. G.-C., Lima, J. A. C., McVeigh, E. R. & Zerhouni, E. A. (1994), Temporal evolution of three dimensional deformation in the ischemic human left ventricle: Assessment by MR tagging, *in* 'Proceedings of the 2nd Annual Meeting of the Society of Magnetic Resonance', Society of Magnetic Resonance Imaging (SMR), Berkely, California, p. 1482. URL: http://prospero.bme-mri.jhu.edu/abstracts/lugo94_1/temporal.html.

Masood, S., Yang, G.-Z., Pennell, D. J. & Firmin, D. N. (2000), 'Investigating intrinsic myocardial mechanics - the role of MR tagging, velocity phase mapping and diffusion imaging', *Journal of Magnetic Resonance Imaging* **12**(6), 873–883.

McCulloch, A. D. & Mazhari, R. (2001), 'Regional ventricular mechanics: Integrative computational models of myocardial flow-function relations', *Journal of Nuclear Cardiology* **8**(4), 506–519. Manuscript available at URL: http://cardiome.ucsd.edu/Publications_files/JNCreview.pdf.

Mirsky, I. & Parmley, W. W. (1973), 'Assessment of passive elastic stiffness for isolated heart muscle and the intact heart', *Circulation Research* **33**(2), 233–243.

Mori, S., Xue, R., Crain, B., Solaiyappan, M., Chacko, V. P. & v. Zijl, P. C. M. (n.d.), 3D reconstruction of axonal fibers from diffusion tensor imaging using fiber assignment by continuous tracking (FACT), *in* 'ISMRM 7th annual scientific meeting, Philadelphia, PA, MAy 22-28, 1999'.

Myers, J. H., Stirling, M. C., Choy, M., Buda, A. J. & Gallagher, K. P. (1986), 'Direct measurement of inner and outer wall thickening dynamics with epicardial echocardiography', *Circulation* **74**(1), 164 – 172.

Reichek, N. (1999), 'MRI myocardial tagging', *Journal of Magnetic Resonance Imaging* **10**(5), 609 – 616. Special Issue: Cardiovascular MRI.

Ruddy, T. D., deKamp, R. A. & Beanlands, R. S. (1999), 'Taking PET to heart', *eCMAJ - Canadian Medical Association Journal, Electronic Edition.* URL: http://www.cma.ca/cmaj/vol-161/issue-9/1131.htm.

Schussheim, A. E., Devereux, R. B., de Simone, G., Borer, J. S., Herrold, E. M. & Laragh, J. H. (1997), 'Usefulness of subnormal midwall fractional shortening in predicting left ventricular exercise dysfunction in asymptomatic patients with systemic hypertension', *The American Journal of Cardiology* **79**(8), 1065 – 1074.

Spitzak, B. (n.d.), 'The FLTK home page', URL: http://www.fltk.org.

van der Geest, R. J. & Reiber, J. H. C. (1999), 'Quantification in cardiac MRI', *Journal of Magnetic Resonance Imaging* **10**(5), 602 – 608. Special Issue: Cardiovascular MRI.

Willenheimer, R., Cline, C., Erhardt, L. & Israelsson, B. (1997), 'Left ventricular atrioventricular plane displacement: an echocardiographic technique for rapid assessment of prognosis in heart failure', *Heart* **78**(3), 230–236.

Wünsche, B. C. (2002*a*), A toolkit for visualizing biomedical data sets, *in* 'Proceedings of GRAPHITE 2003'. (accepted for publication).

Wünsche, B. C. (2002*b*), The Visualization of Tensor Fields in Biological Tissue, PhD thesis, University of Auckland. (To be published).

Wünsche, B. C. & Lobb, R. (2001), The visualization of diffusion tensor fields in the brain, *in* 'Proceedings of METMBS'01', CSREA Press, pp. 498 – 504.

Young, A. A., Dokos, S., Powell, K. A., Sturm, B., McCulloch, A. D., Starling, R. C., McCarthy, P. M. & White, R. D. (2000), 'Regional heterogeneity of function in nonischemic dilated cardiomyopathy', *Cardiovascular Research* **49**(2), 308–318.

Young, A. A., Imai, H., Chang, C.-N. & Axel, L. (1994), 'Two-dimensional left ventricular deformation during systole using magnetic resonance imaging with spatial modulation of magnetization', *Circulation* **89**(2), 740 – 752.

Young, A. A., Kraitchman, D. L., Dougherty, L. & Axel, L. (1995), 'Tracking and finite element analysis of stripe deformation in magnetic resonance tagging', *IEEE Transactions on Medical Imaging* **14**(3), 413 – 421.

Young, A. A., Kramer, C. M., Ferrari, V. A. & ad Nathaniel Reichek, L. A. (1994), 'Three-dimensional left ventricular deformation in hypertrophic cardiomyopathy', *Circulation* **90**(2), 854 – 867.